Article:

Vivacqua, V, López, A, Hammond, R et al. (1 more author) (2019) DEM analysis of the effect of particle shape, cohesion and strain rate on powder rheometry. Powder Technology, 342. pp. 653-663. ISSN 0032-5910

https://doi.org/10.1016/j.powtec.2018.10.034

DEM Analysis of the Effect of Particle Shape, Cohesion and Strain Rate on Powder Rheometry

Vincenzino Vivacqua, Alejandro López, Robert Hammond and Mojtaba Ghadiri*

School of Chemical and Process Engineering, University of Leeds, Leeds LS2 9JT, UK.
*Contact email: m.ghadiri@leeds.ac.uk

Abstract

Discrete Element Method (DEM) is used to simulate the flow of particles addressing the influence of shear strain rate, particle shape and cohesion on the flow characteristics. For this purpose, the dynamics of particle motion in the Freeman Technology FT4 rheometer is analysed. The simulations are first validated by comparison with experiments with cohesive particles, i.e. silanised glass beads, from the literature. Particles with faceted shapes, sharp corners and edges are then simulated and found to require significantly higher energy to flow compared to spherical particles. The presence of truncated vertices, typical of active pharmaceutical ingredients, influences the flow behaviour drastically. The results of this analysis therefore reveal the importance of considering the actual particle shape in DEM simulations when faceted particles are considered. Finally, a rheological model describing the relationship between the dimensionless shear stress and the inertial number for several particle shapes, cohesion values and blade tip speeds is proposed. The outcome of this study may lead to a unified rheological description of powder flow, which incorporates the effect of cohesion, shape and shear strain rate.

Keywords: Flowability, DEM, Freeman FT4, Faceted Particles, Cohesion, Shear Strain Rate

Nomenclature

d_p	Particle size [m]	r_i^c	Branch vector [m]
E	Young's modulus [Pa]	t	Time [s]
$F_{c,i}$	Contact force on particle i [N]	u	Translational velocity of FT4 blade [$\frac{m}{s}$]
F_j^c	Contact force at contact c [N]	U_{tip}	Blade tip velocity [$\frac{m}{s}$]
F_n	Normal elasto-plastic contact force [N]	V	Cell volume [m^3]
F_t	Tangential force [N]	v_i	Translational particle velocity [$\frac{m}{s}$]
g	gravitational acceleration [$\frac{m}{s^2}$]	δ	Overlap [m]
I	Inertial number [-]	δv_i	Fluctuation velocity of particle i [$\frac{m}{s}$]
I_i	Moment of inertia [$kg\ m^2$]	γ	Shear strain rate [$\frac{1}{s}$]
K_{adh}	Elastic stiffness [$\frac{N}{m}$]	Γ	Solid specific surface energy [$\frac{J}{m^2}$]
K_{nl}	Loading stiffness [$\frac{N}{m}$]	ε	Coefficient of restitution [-]
K_{nu}	Unloading stiffness [$\frac{N}{m}$]	μ	Friction coefficient [-]
$M_{c,i}$	Contact torque on particle i [N m]	μ_r	Rolling friction coefficient [-]
m_i	Mass of particle i [kg]	$\overline{\sigma_{ij}}$	Stress tensor [Pa]
m_p	Mass of individual particles in cell volume V [kg]	$\sigma_{1,2,3}$	Principal stresses [Pa]
N_c	Number of contacts [-]	τ	Shear stress [Pa]
N_p	Number of particles [-]	ω_i	Rotational velocity [$\frac{rad}{s}$]
p	Normal stress [Pa]	ω_{rel}	Relative angular velocity [$\frac{rad}{s}$]
R_i	Rotation matrix [-]		

1. Introduction

Assessing the flow properties of powder is crucial to ensure effective transfer between unit operations as well as to obtain a good quality product. Unfortunately, the fundamental understanding of powder flow is still limited and this due to the large number of variables which can affect the phenomenon. Among these variables, particle shape, cohesion and shear strain rate can all influence the flow behaviour.

The study of powder flow as a function of shear strain rate, in particular, is relevant to processes such as fast feeding, dosing, conveying, mixing and packaging processes. However, powder flow characterisation methods are usually based on shear cell tests, which provide measurements only at low values of the shear strain rate, i.e. in the quasi-static flow regime. Extrapolation of these measurements to dynamic conditions can be misrepresentative as the shear stress can vary with shear strain rate in the intermediate and inertial regime. This has been shown, for example, by Tardos et al. [1] while investigating powder flow in a Couette device. Furthermore, conventional shear testers do not provide accurate measurements at normal stresses lower than 1 kPa, whereas there is also a strong need to develop techniques for low levels of consolidation stress, e.g. for dry powder inhalers and die filling [2-4]. The flow properties must therefore be determined while the powder is in motion and at relevant stress and shear strain rate conditions. However, even in the simple Couette geometry, the analysis of the flow pattern is complicated by the presence of a secondary recirculating flow [5-6]. As an alternative to the Couette device, a mechanically stirred powder bed rheometer has been used by Bruni et al. [7] and Tomasetta et al. [8] to study the powder response to shear deformation. A rheological model based on continuum mechanics was developed for this device to describe the powder stress state and the applied torque. However, the vertical position of the rotating impeller is fixed in this device, and therefore the measurements may not be indicative of the whole particle bed, as the flow properties can vary with the bed depth. Furthermore, powder aeration in the narrow high shear strain rate region may adversely affect the results. In the FT4 powder rheometer of Freeman Technology, Tewkesbury, UK [9], information on the powder flowability is obtained by measuring the work required to drive a rotating blade into a powder bed, referred to as 'flow energy'. Unfortunately, there is no theory which can relate this measured flow energy to the stress level inside the powder assembly. This would require the derivation of a rheological law capable of encompassing all flow regimes; attempts in this direction are summarised elsewhere [10-15], but fine cohesive powders are posing the greatest challenge. Therefore, information obtained from the FT4 powder rheometer can be used only for comparative studies between powders.

In order to develop a rheological description of powder flow, information at the particle level must be obtained. This can be done by carrying out simulations based on the Discrete Element Method (DEM). Recently, several studies have focused on the analysis of the powder flow dynamics by numerical simulations. Hare et al. [16] performed DEM simulations of FT4 to calculate the stress and shear strain rate distributions, using a linear elasto-plastic and adhesive contact model to describe the behaviour of glass beads made cohesive by silanisation. They found that the designed twist in the FT4 blade provides a roughly constant shear stress profile along the radial direction across the blade length. Bharadwaj et al. [17] using DEM showed that the flow energy was sensitive to the particle shape and friction coefficients. However, the shear strain rate and the stress within the particle bed were not characterised. Recently Nan et al. [18] simulated the rheological behaviour of polyethylene spherical particles in the FT4 in the presence of an upward gas flow by coupling DEM with Computational Fluid Dynamics (CFD) approach. They found that the flow energy correlates linearly with the shear stress in front of the blade for all conditions including permeating air. They also derived a relationship between the bulk friction coefficient and inertial number similar to that proposed by Chialvo et al. [19] for all flow regimes. This relationship can be regarded as a constitutive law for powder flow in the intermediate flow regime. In a subsequent study, Nan et al. [20] proposed an equation to describe the effect of tip speed on the pseudo-viscosity of particle flow, expressed as a function of the inertial number.

Studies on the rheological behaviour of non-spherical particles are limited [21-25]. Cleary [22] simulated the Couette flow of super-quadric shaped particles with aspect ratio less than 2 and found a much larger shear resistance with this shape than with spheres, due to higher particle interlocking. Soltanbeigi et al. [26] studied the influence of edge sharpness and bumpiness of particles on granular flow and Campbell [21] simulated the simple shear flow of ellipsoidal particles. Si et al. [27] evaluated the effect of particle size and cohesion on flow characteristics. Their results on irregularly shaped limestone particles indicate that there is a median size (around 150 μm) below which cohesion dominates the bulk behaviour. Above this limit, the effect of cohesion decreases monotonically with increasing particle size. The quasi-static / inertial transition occurs at a much smaller solid fraction for ellipsoids than that for spheres, as the formation of force chains is more likely with ellipsoids. Nan et al. [23] studied the rheological behaviour of rod-like particles in an FT4 powder rheometer. The work associated with rodlike particles was found much larger than that of spheres and increasing with the aspect ratio. The flowability of rodlike particles was also found to improve by the addition of spherical beads. These studies reveal the importance of considering the influence of the actual particle shape on the bulk flow behaviour, but are limited to simple shapes such as cylinders or ellipsoids. In this study, the flow behaviour of polyhedra is simulated by using a commercial software Rocky DEM, ESSS, Florianopolis, Brazil. A particular feature of this software package is its ability to simulate faceted particle shape. Crystalline solids, as frequently found, for example, in the pharmaceutical industry, have such type of shape, making the simulation more representative of the real crystal shape. The flow behaviour of both cohesive and free-flowing particles flow is investigated as a function of shear strain rate, with the aim of providing a step forward towards a rheological description of powder flow which incorporates the effect of cohesion, shape and shear strain rate. For this purpose, use is made of FT4 powder rheometer to simulate the dynamic shear strain rate conditions.

2. DEM methodology

DEM modelling is carried out using commercial software package Rocky DEM, provided by ESSS Group. In the Discrete Element Modelling approach originally described by Cundall and Strack [28], movement of individual particles can be described in terms of their translational and rotational motions:

$$m_i \frac{d\boldsymbol{v}_i}{dt} = \sum \boldsymbol{F}_{c,i} + m_i \boldsymbol{g} \quad (1)$$

$$\frac{d(\boldsymbol{I}_i \boldsymbol{\omega}_i)}{dt} = \boldsymbol{R}_i \left(\sum \boldsymbol{M}_{c,i}\right) \quad (2)$$

In equations (1-2), m_i is the mass of the particle, $\mathbf{I}_i$, $\mathbf{v}_i$, $\boldsymbol{\omega}_i$ and $\mathbf{R}_i$ are the moment of inertia, translational and rotational velocities and rotation matrix relating the global and local coordinate systems, respectively. $\mathbf{M}_{c,i}$ is the contact torque as a result of the contact forces and torque arising from rolling friction. The model describing the contact force $\mathbf{F}_{c,i}$ implemented in Rocky is a linear spring hysteresis model with no viscous damping term. In the absence of cohesion, this model can be described by the following set of equations:

$$F_n^t = \min\left(F_n^{t-\Delta t} + K_{nu}\left(\delta_n^t - \delta_n^{t-\Delta t}\right), K_{nl}\,\delta_n^t\right) \qquad \text{if } \left(\delta_n^t - \delta_n^{t-\Delta t}\right) \geq 0 \quad (3)$$

$$F_n^t = \max\left(F_n^{t-\Delta t} + K_{nu}\left(\delta_n^t - \delta_n^{t-\Delta t}\right), 0.001 \cdot K_{nl}\,\delta_n^t\right) \qquad \text{if } \left(\delta_n^t - \delta_n^{t-\Delta t}\right) < 0 \quad (4)$$

where F_n^t is the normal elastic-plastic contact force at the current time, t; $F_n^{t-\Delta t}$ is the force at the previous time; δ_n^t and $\delta_n^{t-\Delta t}$ are the normal overlaps during the current and previous time respectively (assumed to be positive as particles are approaching each other); K_{nl} and K_{nu} are the values of the loading and unloading contact stiffness, respectively. The normal loading and unloading stiffness are calculated as:

$$K_{nl} = \frac{K_{n1} K_{n2}}{K_{n1} + K_{n2}} \quad (5)$$

$$K_{nu}=\frac{K_{nl}}{\varepsilon^2} \quad (6)$$

$$K_{n1,2}= E_{1,2}\ d_{p1,2} \quad (7)$$

where ε is the coefficient of restitution, E is the Young modulus and d_p is the particle size. The subscripts 1 or 2 refer to particles 1 and 2. In case of collision with a boundary, the Young modulus of the boundary is substituted into Eq. 5.

The tangential force F_t^t in Rocky is computed by the following equation:

$$F_t^t = \min\left(F_t^{t-\Delta t} + K_{nl}\left(\delta_t^t - \delta_t^{t-\Delta t}\right), \mu \cdot F_n^t\right) \quad (8)$$

where δ_t^t and $\delta_t^{t-\Delta t}$ are the tangential overlaps during the current and previous time step, respectively, and μ is the friction coefficient (separate values for static and dynamic friction coefficients can be used in Eq.8, the same value for both is used in this study). A rolling torque is introduced based on the relative angular velocity ω_{rel} at the contact point:

$$M_r=-\frac{\omega_{rel}}{|\omega_{rel}|}\mu_r F_n d_p/2 \quad (9)$$

where μ_r is the rolling friction coefficient.

In the presence of cohesion/adhesion, a linear adhesive force model of Luding [29] is used. This force varies linearly with the normal overlap and is defined by K_{adh}, which is the ratio between the adhesive force stiffness and the normal loading stiffness K_{nl}:

$$F^{t}_{n,\,adh} = K_{adh}\, K_{nl}\, (\delta_{n}^{t} - \delta_{n}^{t-\Delta t}) \quad (10)$$

A schematic diagram for the normal force contact model used in Rocky is shown in Figure 1.

3. Model Validation

As a preliminary step, the model presented in the previous section is validated with some experiments reported by Hare et al. [16]. They made particles with sizes ranging between 1.7 and 2 mm cohesive by silanisation. They used different functional groups on the particle surface in order to introduce different levels of surface energy. These particles were then subjected to a standard FT4 downward test, as depicted in Figure 2, in a 50 mm vessel, by rotating a 48 mm impeller anti-clockwise with a tip speed of 100 mm/s and a blade helix angle of 5°. Full blade velocity details are given by Hare et al. [16]. The cumulative energy (work done by penetrating the rotating impeller into the particle bed, termed flow energy) was calculated by integrating the axial profiles of the impeller torque T and of the vertical force F, which are recorded by the FT4:

$$E = \int_{0}^{H} \left(\frac{T}{R\tan(\alpha)} + F \right) dH \quad (11)$$

where R is the radius of the blade; α is the helix angle (5 °C).

They also carried out DEM simulations on the same system by using a more realistic contact model (Pasha et al., [30]). The parameters used in this study are given in Tables 1. They are the same as those used by Hare et al. [16], but in the case here using the contact model available in Rocky. The calculated cumulative energy required to rotate the impeller is reported as a function of the penetration depth in Figure 3 together with the experimental data for comparison.

With non-cohesive glass beads, the model slightly underestimates the experimental values of the flow energy. However, a finer tuning of the sliding friction coefficient, often considered as an adjustable parameter during DEM models calibration, could produce a better agreement. When the experiments with silanised glass beads at varying surface energy are considered, the DEM model is able to reproduce the experimental behaviour by selecting a suitable value for the adhesive stiffness ratio K_{adh}, which can be numerically related to the particle surface energy.

A better agreement could have been obtained by using slightly different values of K_{adh}. The outcome of this analysis reveals that the simplified model used in this study is nevertheless sufficiently predictive of the flow behaviour of cohesive powder. In order to derive a relationship between K_{adh} and the material surface energy, an equation would need to be constructed by equating the work required for detachment, i.e. the area under the curve of Luding's model for the tensile force region [29], and a model of work associated with the surface energy that is relevant to the process; e.g. the full JKR model for adhesive elastic contacts, or the model of Thornton and Ning [31] or Pasha et al. [30], both for elasto-plastic adhesive contacts.

4. Results and Discussion

4.1. Effect of particle shape and size on the flow energy

The analysis carried out in the previous section provided sufficient confidence in the model predictions. Before assessing the effect of particle shape and cohesion, a preliminary sensitivity test with respect to particle size has been performed. The standard FT4 downward test is simulated in a smaller 25 mm vessel and a corresponding 23.8 mm impeller diameter. The blade tip speed is 100 mm/s and the corresponding impeller downward speed is 8.72 mm/s. The outcomes of this analysis for non-cohesive spheres are shown in Figure 4. The flow energy is approximately the same with either 1 mm or 2 mm particles, while a significantly higher flow energy is computed for larger particles. This is probably due to the effect of walls which becomes important as the particle size becomes comparable to the column diameter. If a larger vessel for 3 mm particles were to be used, a lower flow energy would be expected.

In the following simulations, more complex particle shapes are considered. Figure 5 shows the flow energy for different sizes of non-cohesive paracetamol-shaped particles. The flow energy is expected to increase as the size decreases. However, the calculated values for 2 mm and 0.8 mm particles are very similar. The higher value obtained for the particles with 2 mm equivalent diameter is likely to be a result of a higher degree of jamming with the blade as well as increased interlocking between particles.

In Figure 6, it is shown that the flow energy associated with shearing of elongated particles is much higher than what is required for spheres. Two types of elongated particles are considered: 1) rounded cylinders, i.e. capsules with an aspect ratio equal to 3; 2) faceted particles (deltahedron shape) with the same aspect ratio but presenting a large number of faces (=16) and corresponding corners (=10), depicted in Figure 7. The flow energy calculated for faceted particles turns out to be significantly larger than that for cylinders. This is due to the presence of sharp-edges which can lead to an increase in particle interlocking and accordingly to a poorer flow behaviour. This will be analysed in more detail further below.

Faceted shapes are a common feature of crystalline solids and are ubiquitous in many active pharmaceutical ingredients (API). Here, the behaviour of particles with a shape similar to that of paracetamol has been simulated. The theoretical paracetamol shape, obtained from molecular dynamic simulations, is complex because it is characterised by a large number of faces (=25) and edges (=44), as depicted in Figure 7a. However, if the very small triangular faces are ignored, the number of major faces is 16. An SEM image of real paracetamol crystals produced in the laboratory by Turner [32] has been included as Figure 7f for reference. The paracetamol shape reported in Fig 7a, is a theoretical one obtained from molecular dynamic simulations and provided by Pickering [33] as an STL file as supplementary material.

In order to identify which features are more important in determining the flow behaviour, the flow energy associated with the actual paracetamol shape is compared with those corresponding to some polyhedra with approximately the same aspect ratio and the same equivalent volume, namely: a truncated polyhedron obtained by enlarging the small triangular faces which are present in the paracetamol structure (Figure 7(b)); deltahedra with the same number of faces as the major faces of the actual paracetamol shape but with less corners (Figure 7(c)); dodecahedra (Figure 7(d)) and cylinders which are equivalent between each other in terms of number of corners and faces. The truncated polyhedron shape is made of two square faces, four hexagonal faces and eight triangle faces with all the edges of the same length. For the theoretical paracetamol shape, an STL file is provided as supplementary material. The comparison of the flow behaviour of these shapes in terms of calculated flow energy is reported in Figure 8. In general, faceted shapes require more energy to flow compared to spheres. Dodecahedra and faceted cylinders require different amounts of energy to flow, although the same number of faces and corners are present in both structures. Deltahedra are characterised by the lowest number of corners and a lower number of faces than the theoretical paracetamol shape. They are the most energy-demanding shapes, probably because of the presence of very sharp corners, which are a result of the low angle between the planes of the different faces that converge on each of the vertices. A measure of sharpness is given by the solid angle, which for a platonic solid can be calculated as:

$$\omega = 2\pi - q(\pi - \theta) \tag{12}$$

where θ is dihedral angle (angle between two intersecting faces) and q is the number of edges meeting at one vertex. For a dodecahedron ($q=3$, $\theta=116.6$ °), the solid angle is equal to about 2.96 steradians, whereas for an octahedron ($q=4$, $\theta=109.5$ °) it is equal to about 1.36 steradians (this octahedron solid angle is the same as the one relevant to the sharpest corner of the deltahedra with 16 faces).

The flow energy seems therefore mainly to be dependent on the sharpness of the corners and few sharp edges can bring about a large reduction in flowability. On the other hand, the behaviour of truncated polyhedra is almost equivalent in terms of flow energy to the actual paracetamol structure. This means that the presence of truncated vertices has an important effect on the powder flow behaviour. The results of this analysis also suggest that shape representation based on clumping together smaller spheres may not be sufficiently representative of the behaviour of particles with sharp edges.

4.2. Effect of combined particle cohesion and shape on the flow energy

In the previous section, an equivalence in terms of flow energy was established between the actual paracetamol shape and that of a truncated polyhedron. However, this equivalence may not hold when cohesion is added to the particles. The flow energy calculated for these two shapes at different values of adhesive stiffness K_{adh} is reported in Figure 9.

At low cohesion level, the energy requirements remain similar, but as the cohesion is increased the difference in flow energy associated with the two shapes widens. A closer inspection reveals that it is mainly due to the presence of local abrupt changes in the slope for truncated polyhedra. This trend corresponds to peaks in the power versus penetration depth diagram shown in Figure 10. In order to calculate the flow energy from the power measurements, the integral of the power with respect to time needs to be calculated. A tentative explanation of the presence of these peaks may stem from the fact that jamming or cluster formation can be enhanced in the presence of large flat conforming contact surfaces. However, this may also be an artefact of the limited number of particles considered in the simulation.

Finally, a mixture of equal number of faceted particles with the same shape (truncated polyhedral) but different levels of cohesion is considered. This system can be of interest for APIs with a distribution of surface energies on the individual facets. The systems studied have the same average level of cohesion, i.e. the mass weighted average of K_{adh} is equivalent for all of them, but one system has a single value, the second a dual value and the third a five-value K_{adh} as shown Figure 11. The calculated flow energies only differ in the single K_{adh} case, for which again an abrupt change in slope is observed. A detailed description of the surface energy distribution among facets of a crystal may not therefore be required for predicting flow behaviour.

4.3. Stress and strain analyses

The flow energy for non-cohesive spheres is calculated for different impeller speeds and presented in Figure 12. It should be noted that the impeller rotational velocity is related to the vertical downward velocity by the helix angle. The values of the downward translational velocity u and angular velocity ω corresponding to the tip speed velocity U_{tip} are given in Table 2.

An increase in the rotational speed does not bring about a significant increase in the flow energy at low speeds. However, the flow energy starts to increase at higher speeds and this is an indication that the transition to a different flow regime is occurring. In order to obtain a description of the flow behaviour across different flow regimes, a stress analysis has been carried out. For this purpose, an average stress tensor is calculated in a volume which encompasses the blades and moves with it at the same vertical velocity. The stress tensor is made up of two components: the first depends on the particle velocity fluctuations and becomes important in the rapid flow regime; the second one sums up all the contact forces between all the particles in this volume [34]. Mathematically, it is expressed as:

$$\bar{\sigma}_{ij} = \frac{1}{2V}\sum_{N_p \in V}\frac{1}{2}m_p \delta v_i \delta v_j + \frac{1}{V}\sum_{N_c \in V} r_i^c F_j^c \tag{13}$$

where V is the cell volume; m_p is the mass of particle p; δv_i and δv_j are the fluctuation velocities of particle p; F^c_j is the contact force at contact c and r_i^c is the corresponding branch vector, N_p is the number of particles and N_c is the number of contacts.

The eigenvalues of the stress tensor $\sigma_{i=1,2,3}$, called principal stresses can be used to calculate the normal stress p and shear stress τ as:

$$p = -\frac{(\sigma_1 + \sigma_2 + \sigma_3)}{3} \tag{14}$$

$$\tau = \frac{\sqrt{(\sigma_1 - \sigma_2)^2 + (\sigma_1 - \sigma_3)^2 + (\sigma_2 - \sigma_3)^2}}{\sqrt{6}} \tag{15}$$

In Figure 13, the average shear stress is plotted as a function of the impeller tip speed for spheres. It is obtained by averaging the value given by Eq. (15) in the cylindrical volume which encompasses the impeller blade (Fig. 14) during the entire downward FT4 test. The slope of the curve in the logarithmic plot shown in Figure 13 clearly changes at the tip speed around 0.1 m/s, indicating a transition from the quasi-static regime, where the stresses are independent of the shear strain rate (the letter is proportional to the tip speed), to the intermediate regime, where the stresses increase with the shear strain rate. These results are consistent with the trend in Figure 12, suggesting that flow energy and stresses are correlated, as also shown by Nan et al. [18 and 20].

A simplified approach is used to calculate the shear strain rate, in analogy with continuum mechanics, based on the particle velocity gradient across a distance in front of the impeller blade. The particle velocity is maximum in the region close to the impeller tip [18] and decays to zero within a relatively narrow region called shear band. It is approximately equal to five particles diameters [16, 35-36]. The shear strain rate is therefore calculated as the ratio between the maximum particle velocity, calculated in the volume which encompasses the impeller blade, and the shear band width.

In the case of a simple plane shear deformation of a granular system, it has been shown, from dimensional and numerical analyses, that the system is controlled by a dimensionless group, called the inertial number ([12, 14, 37-39]), as defined by Equation 16. It is the ratio between the inertial time scale and the external time scale:

$$\mathrm{I} = d_p \gamma \sqrt{\frac{\rho_p}{p}} \tag{16}$$

where ρ_p is the particle density. In the case of simple plane shear, the following phenomenological law relating the bulk friction coefficient to the inertial number has been proposed [12]:

$$\mu = \frac{\tau}{p} = \mu_1 + \frac{\mu_2 - \mu_1}{I_0/I + 1} \tag{17}$$

with μ_1, μ_2 and I_0 as fitting constants. μ_1 represents the bulk friction coefficient in the quasi-static regime, whereas μ_2 is an asymptotic value corresponding to large inertial numbers, the existence of which is supported by experiments of steady granular fronts flowing down a slope [37]. In Figure 15, it is shown that Eq. 17 is approximately valid to describe the shear flow of non-cohesive spheres. In Figure 16, the same phenomenological law is applied to faceted particles (deltahedra). The trend of the simulation data fits nicely Eq. 17 at low values of the inertial number but not for the high values. Moreover, when cohesion is introduced even when the particles are spherical the approach is no longer predictive (Figure 17). The fact that the simple rheology expressed by Eq.17 cannot describe the cohesive flow behaviour is somehow expected. The inertial number alone cannot completely define the rheology of cohesive system, but an additional parameter including cohesion has to be taken into account [17, 38-39], requiring further development.

In Figures 18-20, the apparent viscosity is plotted as a function of the inertial number for non-cohesive spheres, non-cohesive deltahedra and cohesive spheres with K_{adh}=0.1, respectively. In agreement with trends reported by Nan et al. [40], an approximate linear relationship is obtained on a logarithmic plot for non-cohesive spheres (Figure 18) having a slope in the range -1.5 to -2.0. A similar behaviour is also found with faceted particles (Figure 19), whereas cohesive spheres (Figure 20) show substantial deviations from the expected trend at some tip speeds, perhaps as a result of episodic clustering or jamming.

It should be noted that the slope of the lines of Figures 18-20 does not change significantly and this suggests the possibility of deriving a generalised correlation for the shear stress τ normalised by the inertial stress $\rho_p d_p^2 \gamma^2$ for a given sliding friction and restitution coefficients and voidage. If this dimensionless shear stress is plotted as a function of the inertial number I for non-cohesive spheres and faceted particles, Figure 21 is obtained. All the data collapse remarkably on a single straight line for faceted particles and on a separate line for non-cohesive spheres with almost the same slope. The difference between polyhedra shapes and spheres mainly changes the intercept of the lines, while the slope is approximately the same, implying that unification of the behaviour with respect to shear strain rate and shape may be possible.

The relationships plotted in Figure 21 for non-cohesive particles are obtained by regression and are expressed as:

$$\frac{\tau}{\rho_p d_p^2 \gamma^2} = 0.481 I^{-1.743} \tag{18}$$

$$\frac{\tau}{\rho_p d_p^2 \gamma^2} = 0.918 I^{-1.754} \tag{19}$$

for sphere and polyhedral shapes, respectively. Equations 18-19 can be regarded as constitutive laws for powder flow valid in the intermediate flow regime, which is found in most applications. The above equations imply that the shear stress is proportional to the shear strain rate to a power index of about 0.25 for both spheres and polyhedral shapes.

In Figure 22, the dimensionless shear stress is plotted as a function of the inertial number for spheres with different adhesive stiffness K_{adh}. Notwithstanding a more scattered behaviour, probably due to appreciable variations in bed voidage, the data still follow approximately a linear trend with the straight lines shifted upward as cohesion is increased.

The correlations in Figure 22 for adhesive particles with K_{adh}=0.1 and 0.2, respectively, are expressed as:

$$\frac{\tau}{\rho_p d_p^2 \gamma^2} = 0.631 I^{-1.801} \tag{20}$$

$$\frac{\tau}{\rho_p d_p^2 \gamma^2} = 1.395 I^{-1.743} \quad (21)$$

In conclusion, faceted shapes and adhesion change the incipient yielding behaviour and have almost no influence on the apparent viscosity in shear deformation.

5. Conclusions

DEM simulations of the shear deformation using the FT4 testing procedure have been carried out addressing the effects of particle shape, cohesion and shear strain rate. It has been found that particle shape can significantly affect the ability of powder to flow, with faceted shapes requiring much higher flow energy compared to spherical particles. In the presence of sharp corners, a sufficiently accurate description of the particle shape is required. However, some shape features appear to have a more important role in determining the flow behaviour. For example, the polyhedral shape with truncated corners can simulate adequately the behaviour of paracetamol, whilst deltahedra with sharp vertices exhibit much larger flow resistance. Also, a detailed description of the surface energy distribution among the facets of a crystal may not be required to reproduce the flow behaviour.

Considering the dynamics of particle motion in an FT4, stresses and flow energy in a FT4 are correlated. The bulk friction coefficient can be expressed as a function of the inertial number for non-cohesive systems. The apparent shear viscosity varies almost linearly on a logarithmic plot with the inertial number having a slope in the range -1.5 to -2.0. The relationship between non-dimensional shear stress and the inertial number is similar for all the systems investigated, regardless of particle shape and level of cohesion. In the light of these findings, a unified rheological description which incorporates the effect of cohesion, shape and shear strain rate may be possible.

Acknowledgement

The authors gratefully acknowledge the support of the Advanced Manufacturing Supply Chain Initiative through the funding of the 'Advanced Digital Design of Pharmaceutical Therapeutics' (Grant No. 14060) project within which the work reported was conducted. The authors would also like to thank Dr Tom Turner for providing a sample of paracetamol crystals and Dr Jonathan Pickering for the stl file of the predicted shape of the same.

References

[1] G.I. Tardos, S. McNamara, I. Talu, Slow and intermediate flow of a frictional bulk powder in the Couette geometry, Powder Technol. 131 (2003) 23–39.

[2] Pasha, M., Hare, C., Hassanpour, A., Ghadiri, M., 2013. Analysis of ball indentation on cohesive powder beds using distinct element modelling. Powder Technology 233, 80-90.

[3] Wang, C., Hassanpour, A., Ghadiri, M., 2008. Characterisation of flowability of cohesive powders by testing small quantities of weak compacts. Particuology 6, 282-285.

[4] Wu, C.Y., Guo, Y., 2012. Numerical modelling of suction filling using DEM/CFD. Chemical Engineering Science 73, 231-238.

[5] Gutam, K.J., Mehandia, V., Nott, P.R., 2013. Rheometry of granular materials in cylindrical Couette cells: Anomalous stress caused by gravity and shear. PHYSICS OF FLUIDS 25, 070602.

[6] Kumar, V.S., Murthy, T., Nott, P.R., 2013. Rheometry of dense granular materials: the crucial effects of gravity and confining walls. Powders and Grains 2013 1542, 49-51.

[7] Bruni, G., Barletta, D., Poletto, M., Lettieri, P., 2007. A rheological model for the flowability of aerated fine powders. Chemical Engineering Science 62, 397-407.

[8] Tomasetta, I., Barletta, D., Lettieri, P., Poletto, M., 2012. The measurement of powder flow properties with a mechanically stirred aerated bed. Chemical Engineering Science 69, 373-381

[9] Freeman, R., 2007. Measuring the flow properties of consolidated, conditioned and aerated powders - A comparative study using a powder rheometer and a rotational shear cell. Powder Technology 174, 25-33.

[10] Campbell, C.S., 2004. Granular Flows and Gas Fluidization. International Journal of Chemical Reactor Engineering 2.

[11] Campbell, C.S., 2006. Granular material flows – An overview. Powder Technology 162, 208-229.

[12] Jop, P., Forterre, Y., Pouliquen, O., 2006. A constitutive law for dense granular flows. Nature 441, 727–730.

[13] Mort, P., Michaels, J.N., Behringer, R.P., Campbell, C.S., Kondic, L., Langroudi, M.K., Shattuck, M., Tang, J., Tardos, G.I., Wassgren, C., 2015. Dense granular flow – A collaborative study. Powder Technol. 284, 571–584.

[14] Pouliquen, O., Cassar, C., Jop, P., Forterre, Y., Nicolas, M., 2006. Flow of dense granular material: towards simple constitutive laws. Journal of Statistical Mechanics-Theory and Experiment 2006, P07020-P07020.

[15] Favier de Coulomb, A., Bouzid, M., Claudin, P., Clément, E., Andreotti, B., Rheology of granular flows across the transition from soft to rigid particles, Physical Review Fluids 2, 2017, 102301(R).

[16] Hare, C., Zafar, U., Ghadiri, M., Freeman, T., Clayton, J., Murtagh, M.J., 2015. Analysis of the dynamics of the FT4 powder rheometer. Powder Technology 285, 123-127.

[17] Bharadwaj, R., Ketterhagen, W.R., Hancock, B.C., 2010. Discrete element simulation study of a Freeman powder rheometer. Chemical Engineering Science 65, 5747-5756.

[18] Nan, W., Ghadiri, M., Wang, Y., 2017a. Analysis of powder rheometry of FT4: Effect of air flow. Chem. Eng. Sci. 162, 141–151.

[19] Chialvo, S., Sun, J., Sundaresan, S., 2012. Bridging the rheology of granular flows in three regimes. Phys. Rev. E: Stat., Nonlin, Soft Matter Phys. 85, 021305.

[20] Nan, W., Ghadiri, M., Wang, Y., 2017b. Analysis of powder rheometry of FT4: Effect of particle shape. Chem. Eng. Sci. 173, 374–383.

[21] Campbell, C.S., 2011. Elastic granular flows of ellipsoidal particles. Phys. Fluids 23, 013306.

[22] Cleary, P.W., 2008. The effect of particle shape on simple shear flows. Powder Technol. 179, 144–163.

[23] Nan, W., Ghadiri, M., Wang, Y., 2017c. Analysis of powder rheometry of FT4: Effect of particle shape. Chem. Eng. Sci. 173, 374-383.

[24] Guo, Y., Wassgren, C., Hancock, B., Ketterhagen, W., 2012. A numerical study of granular shear flows of rod-like particles using the discrete element method. Journal of Fluid Mechanics 713, 1-26.

[25] Haertl, J., Ooi, J. Y., 2011. Numerical investigation of particle shape and particle friction on limiting bulk friction in direct shear tests and comparison with experiments, Powder Technology, 212, 231-239.

[26] Soltanbeigi, B., Podlozhnyuk, A., Papanicopulos, S. A., Kloss, C., Pirker, S. and Ooi, J., 2018. DEM study of mechanical characteristics of multi-spherical and super-quadratic particles at micro and macro scales, Powder Technology 329, 288-303.

[27] Si, H., Mohanty, R., Chakravarty, S., Cabiscol, R., Morgeneyer, M., Zetzener, H., Ooi, J., Kwade, A., Luding, S., Magnanimo, V., 2018. Effect of particle size and cohesion on powder yielding and flow, Kona Powder and Particle Journal, 35, 226-250.

[28] P.A. Cundall, O.D.L. Strack, 1979. A discrete numerical model for granular assemblies. Géotechnique, 29 (1979), pp. 47-65

[29] Luding, S., 2008, Cohesive frictional powders: contact models for tension. Granular Matter, 10:235-246.

[30] Pasha, M., Dogbe S., Hare, C., Hassanpour, A., Ghadiri, M., 2014. A new linear contact model for elasto-plastic and adhesive contacts in distinct element method, Granul. Matter 16, 151–162.

[31] Thornton, C., Ning, Z., 1998. A theoretical model for the stick/bounce behaviour of adhesive elastic–plastic spheres. Powder Technol. 99, 154–162.

[32] Turner, T., 2018. Personal communication.

[33] Pickering, J., 2018. Personal communication.

[34] Bagi, K., 1996. Stress and strain in granular assemblies. Mechanics of materials, 22, 165-177.

[35] Remy, B., Khinast, J.G., Glasser, B.J., 2009. Discrete Element Simulation of Free Flowing Grains in a Four-Bladed Mixer. AICHE Journal, 55, 2035-2048.

[36] Remy, B., Khinast, J.G., Glasser, B.J., 2011. Polydisperse granular flows in a bladed mixer: Experiments and simulations of cohesionless spheres. Chemical Engineering Science 66, 1811-1824.

[37] Pouliquen, O., 1999. On the shape of granular fronts down rough inclined planes. Phys. Fluids, 11, 1956-1958.

[38] Rognon, P., Roux, J-N., Naaïm, M., Chevoir, F., 2007. Dense flows of bidisperse assemblies of disks down inclined plane, Phys. Fluids, 19, 058101.

[39] Berger, N., Azéma, E., Douce, J. F., Radjai, F., 2015. Scaling Behaviour of cohesive granular flows, EPL, 112, 64004.

[40] Nan, W., Vivacqua, V., Ghadiri, M., Wang, Y., 2017c. Numerical analysis of air effect on the powder flow dynamics in the FT4 Powder Rheometer. Powders & Grains 2017, EPJ Web of Conferences epjconf 140, 03036 (2017), DOI: 10.1051/epjconf/201714003036

Table 1: DEM parameters and interaction properties used in Hare et al. (2015)

Material Property	Particles	Geometry
Density (kg/m^3)	2450	7800
Young Modulus (GPa)	0.1	100

Interaction Property	Particles-particles	Particle-geometry
Restitution coefficient (no cohesion)	0.8	0.8
Restitution coefficient (with cohesion)	0.4	0.4
Sliding friction coefficient	0.3	0.1
Rolling friction coefficient	0.01	0.01

Table 2. Values of the translation and rotational velocity.

U_{tip}, m/s	0.025	0.05	0.10	0.25	0.50	1.00
u, mm/s	2.18	4.36	8.72	21.8	43.6	87.2
ω, rad/s	2.12	4.24	8.48	21.2	42.4	84.8

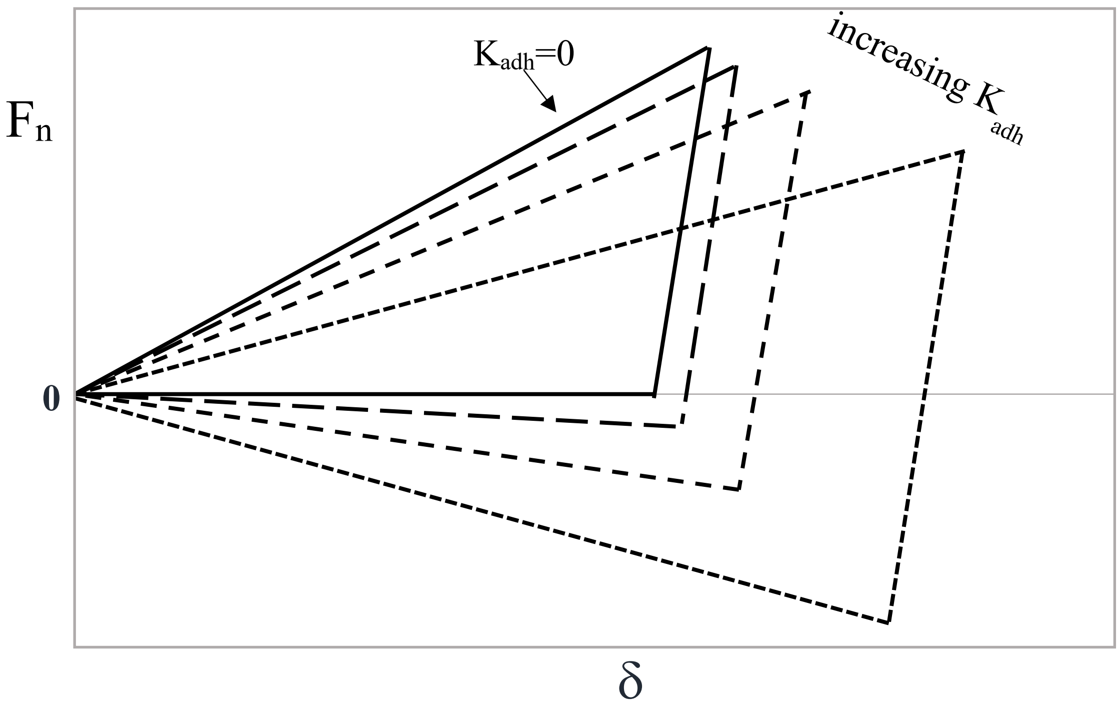

Figure 1: Schematic diagram of the normal force vs overlap relationship according to the contact model used in Rocky.

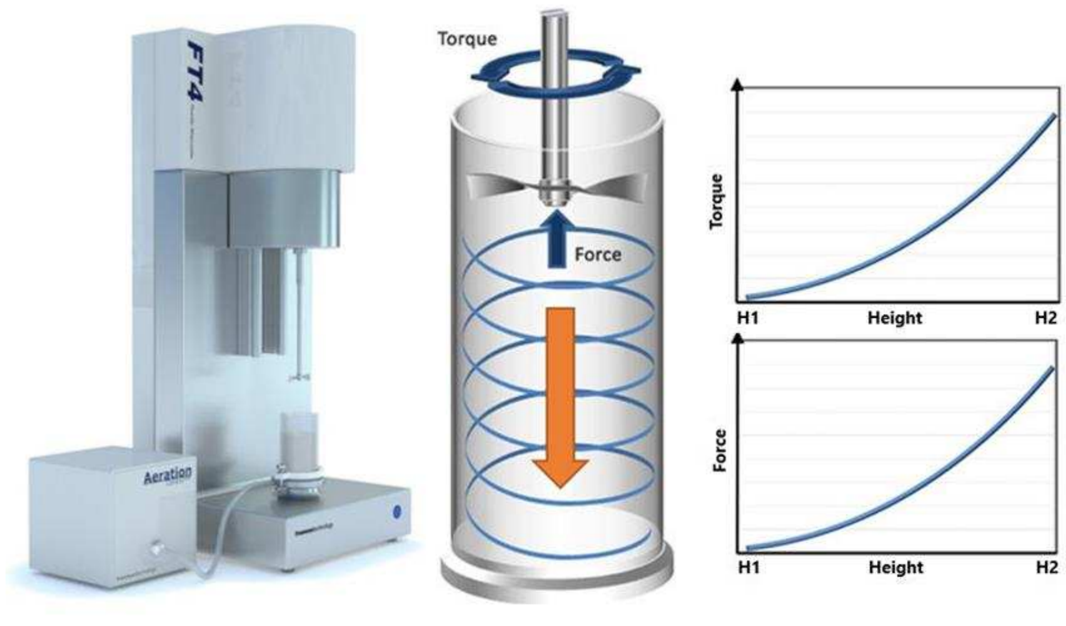

Figure 2: Image of the FT4 Rheometer, schematic of the path followed by the blade tip and average representation of the resulting graphs for torque and force [9].

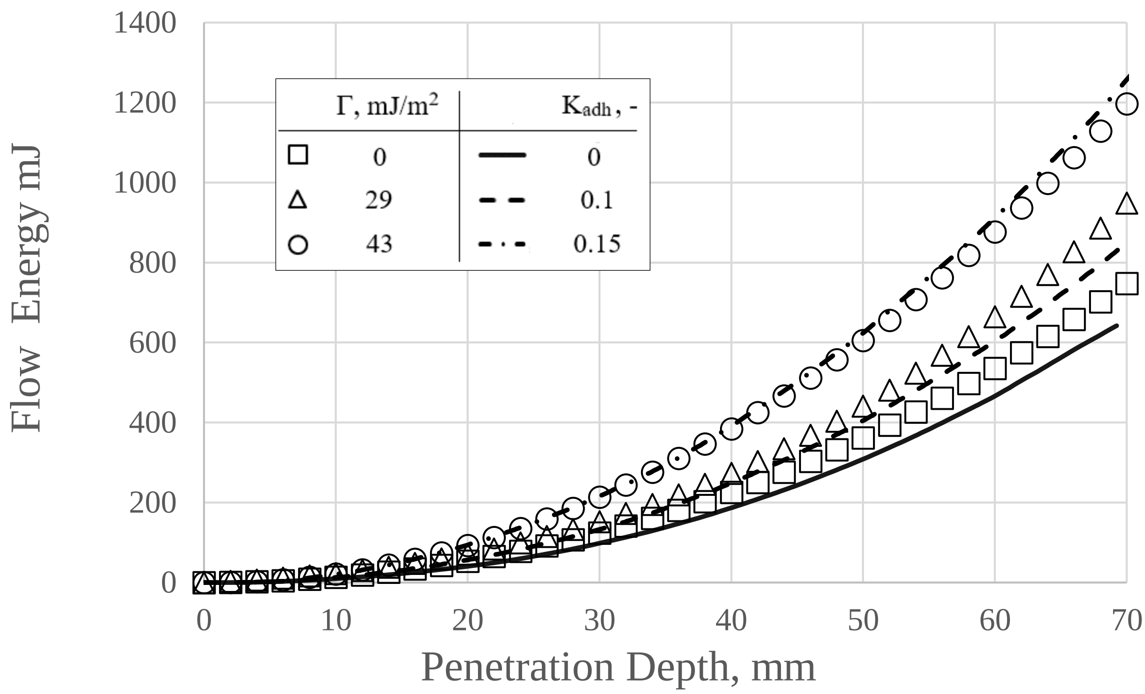

Figure 3: Comparison between calculated and experimental flow energy for silanised glass beads with different values of surface energy in the 50 mm vessel of the FT4 rheometer.

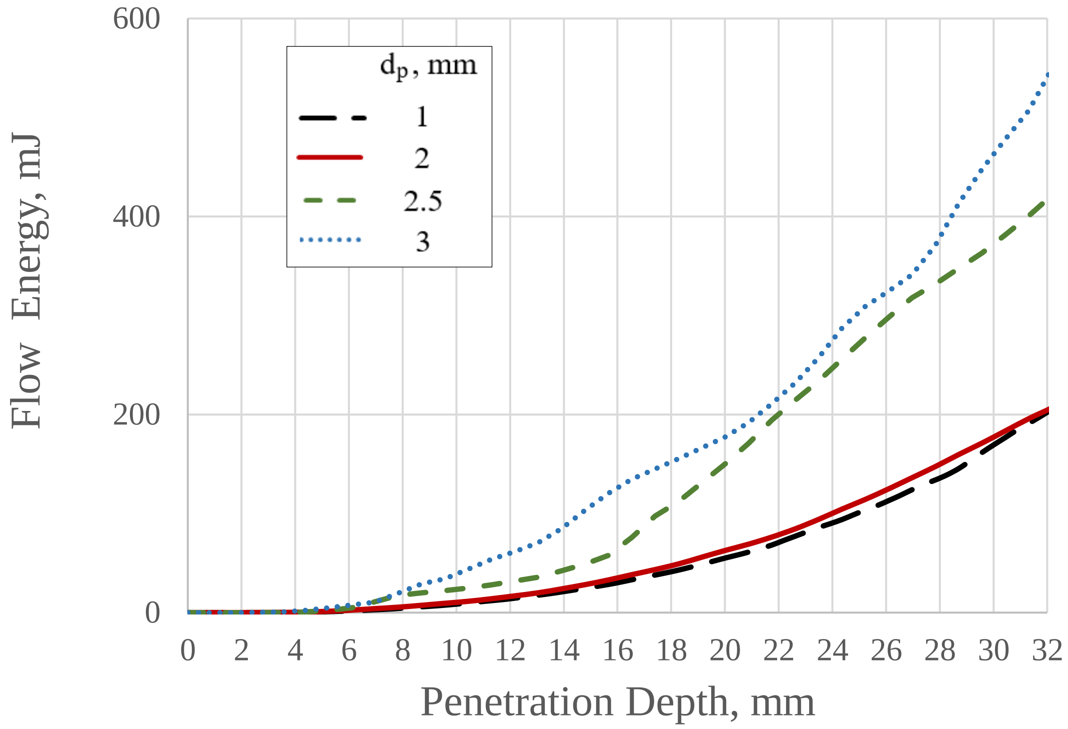

Figure 4: Effect of particle size on the calculated flow energy for non-cohesive spheres in the 25 mm vessel of the FT4 rheometer.

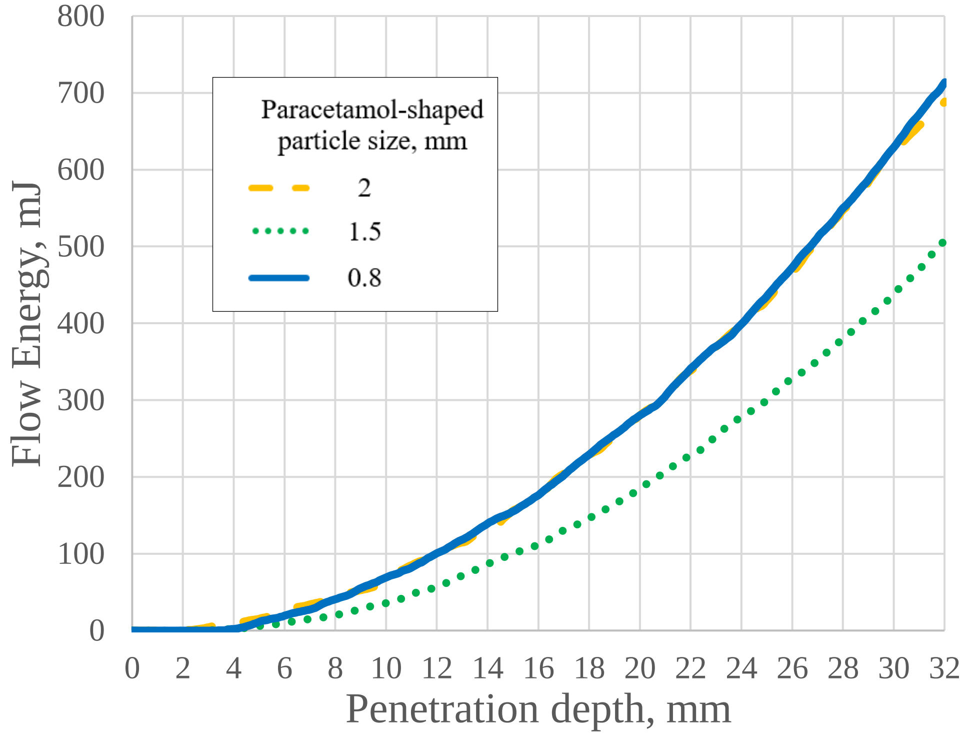

Figure 5: Effect of particle size on the calculated flow energy for non-cohesive Paracetamol-shaped particles in the 25 mm vessel of the FT4 rheometer.

1 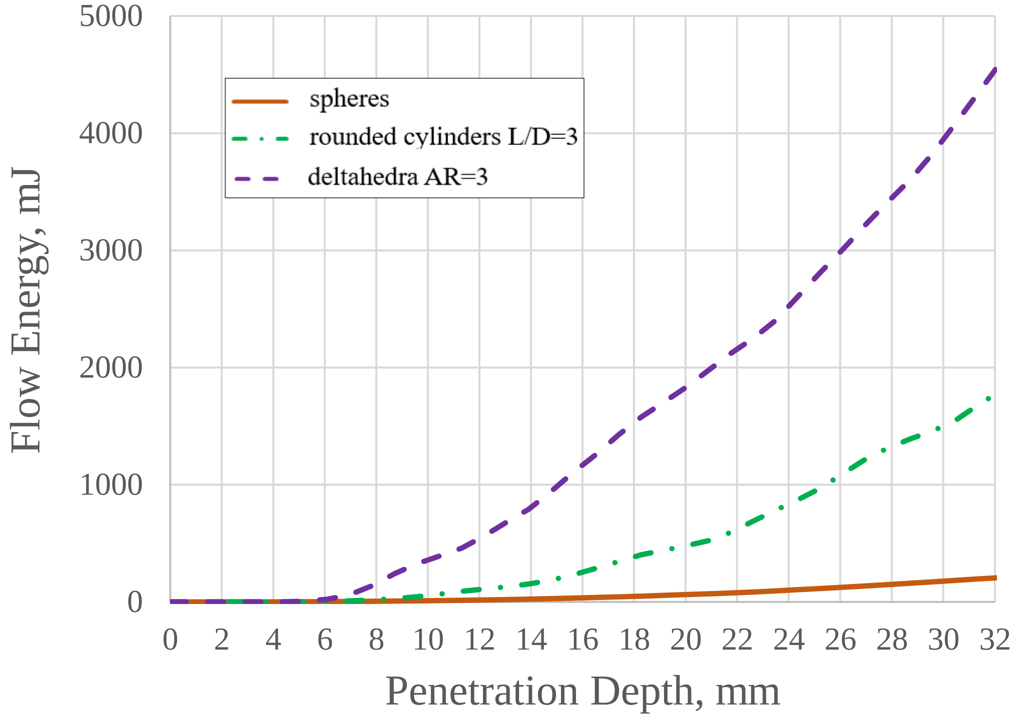

2 **Figure 6:** Comparison between calculated flow energy for spheres, rounded cylinders (AR=3)

3 and faceted particles (AR=3) (25 mm vessel of the FT4 rheometer).

4

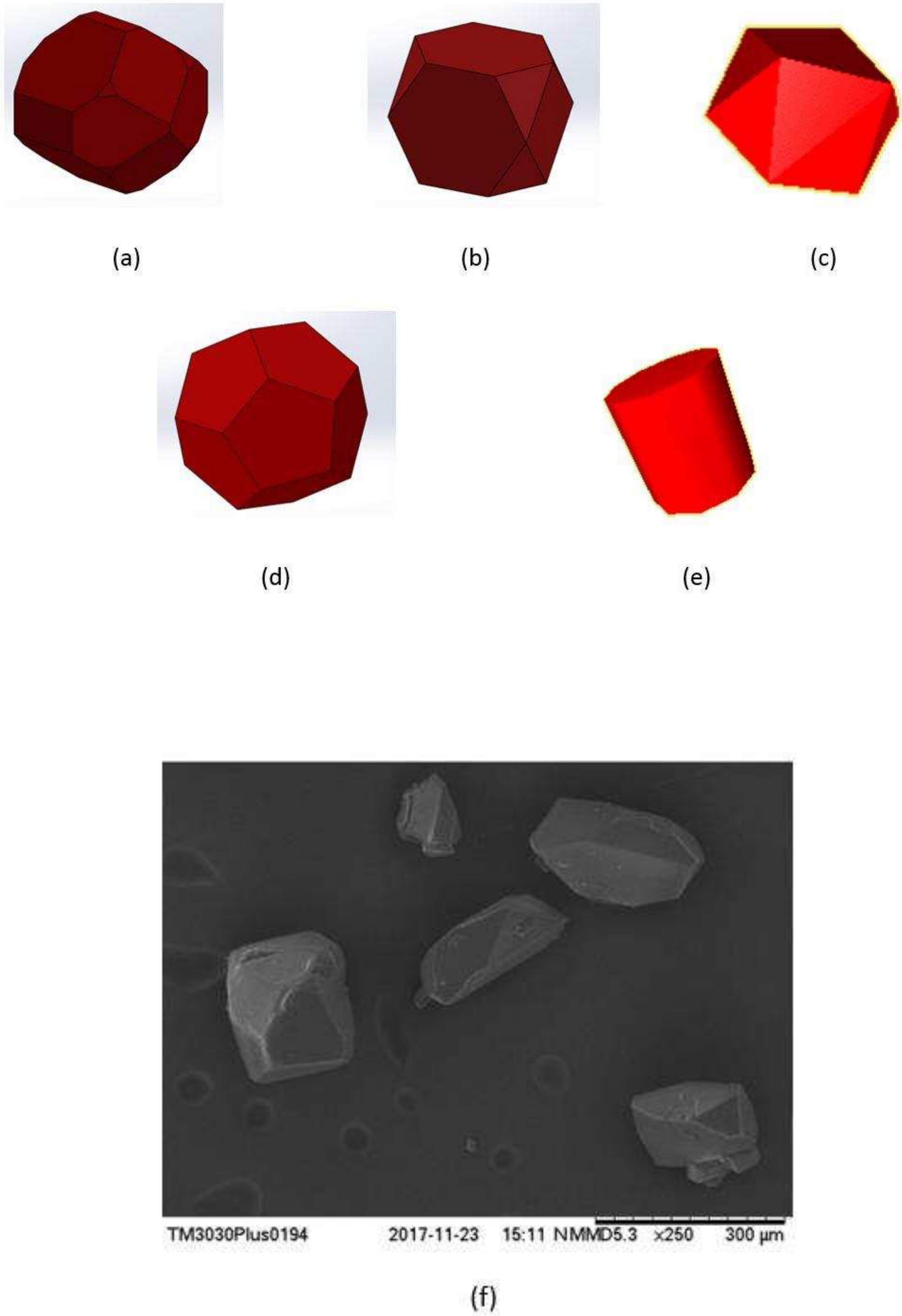

Figure 7: Faceted particles simulated: a) theoretical paracetamol shape (faces=25, corners=44); b) truncated polyhedron (faces=14, corners=16); c) deltahedron (faces=16, corners=10); d)

dodecahedron (faces=12, corners=20); e) faceted cylinder (faces=12, corners=20); f) real paracetamol SEM image (Hitachi Benchtop TM3030 Scanning Electron Microscope).

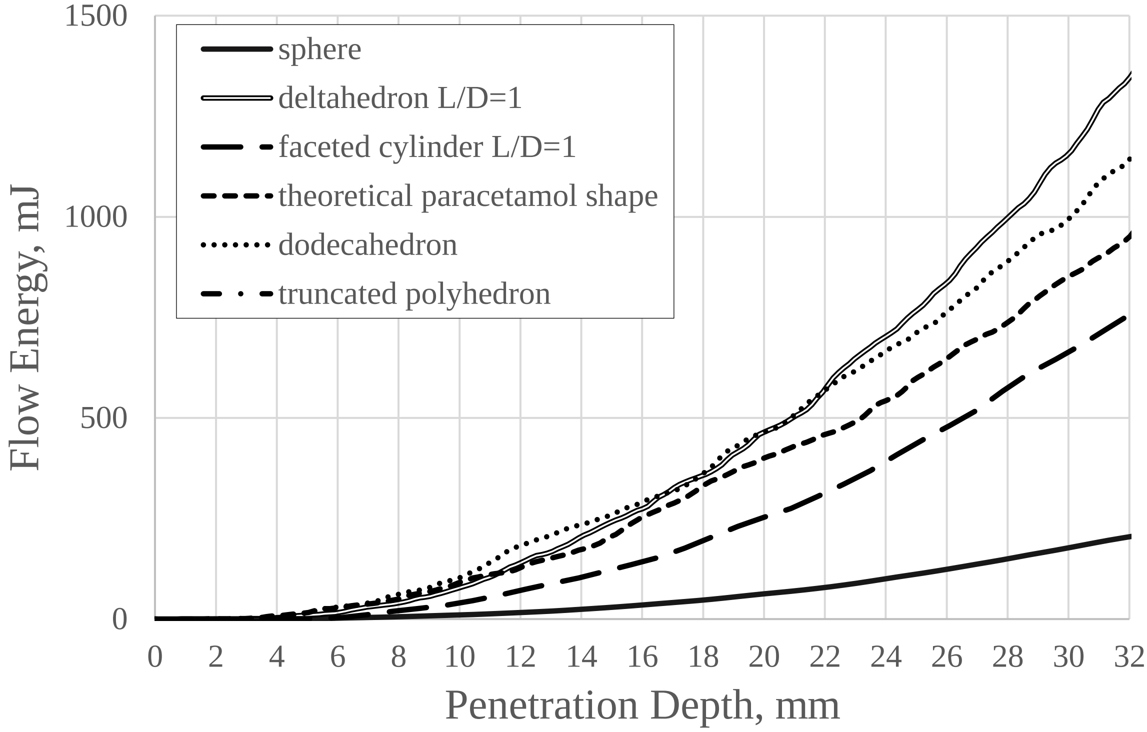

Figure 8: Comparison of flow energy of the particle shapes described in Figure 6: (a) theoretical paracetamol shape, (b) truncated polyhedron, (c) deltahedron, (d) dodecahedron, (e) faceted cylinder (25mm vessel of the FT4 rheometer).

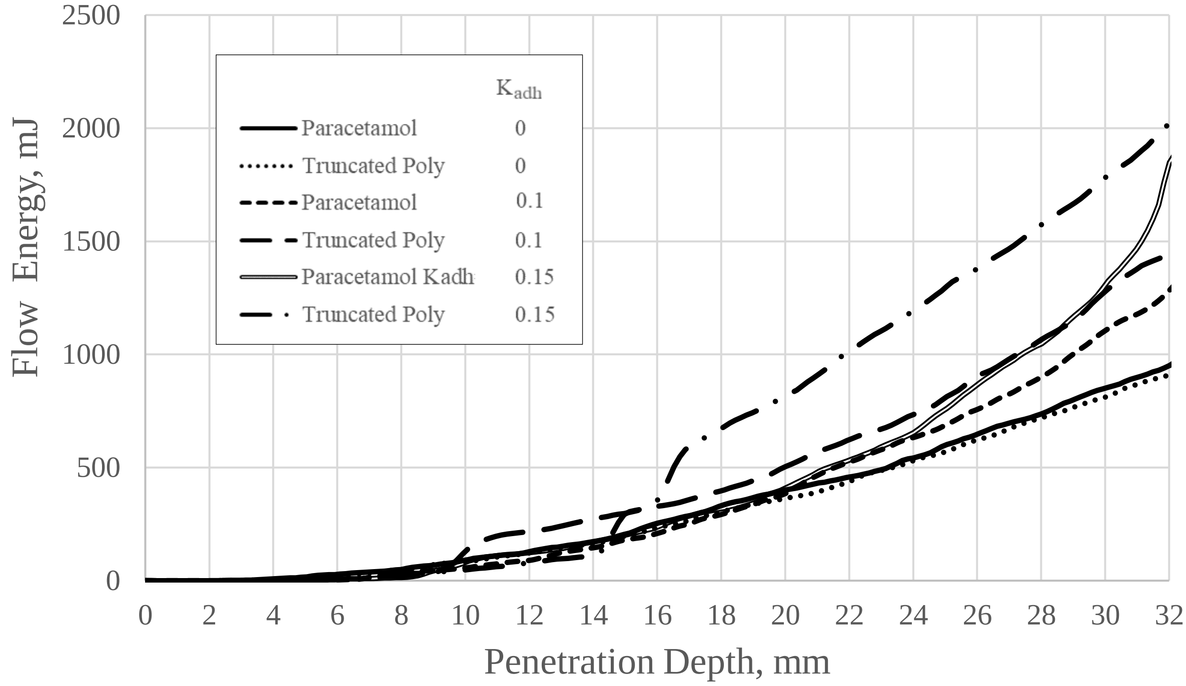

Figure 9: Comparison of flow energy of truncated polyhedra and paracetamol shapes at different levels of cohesion (25 mm vessel of the FT4 rheometer).

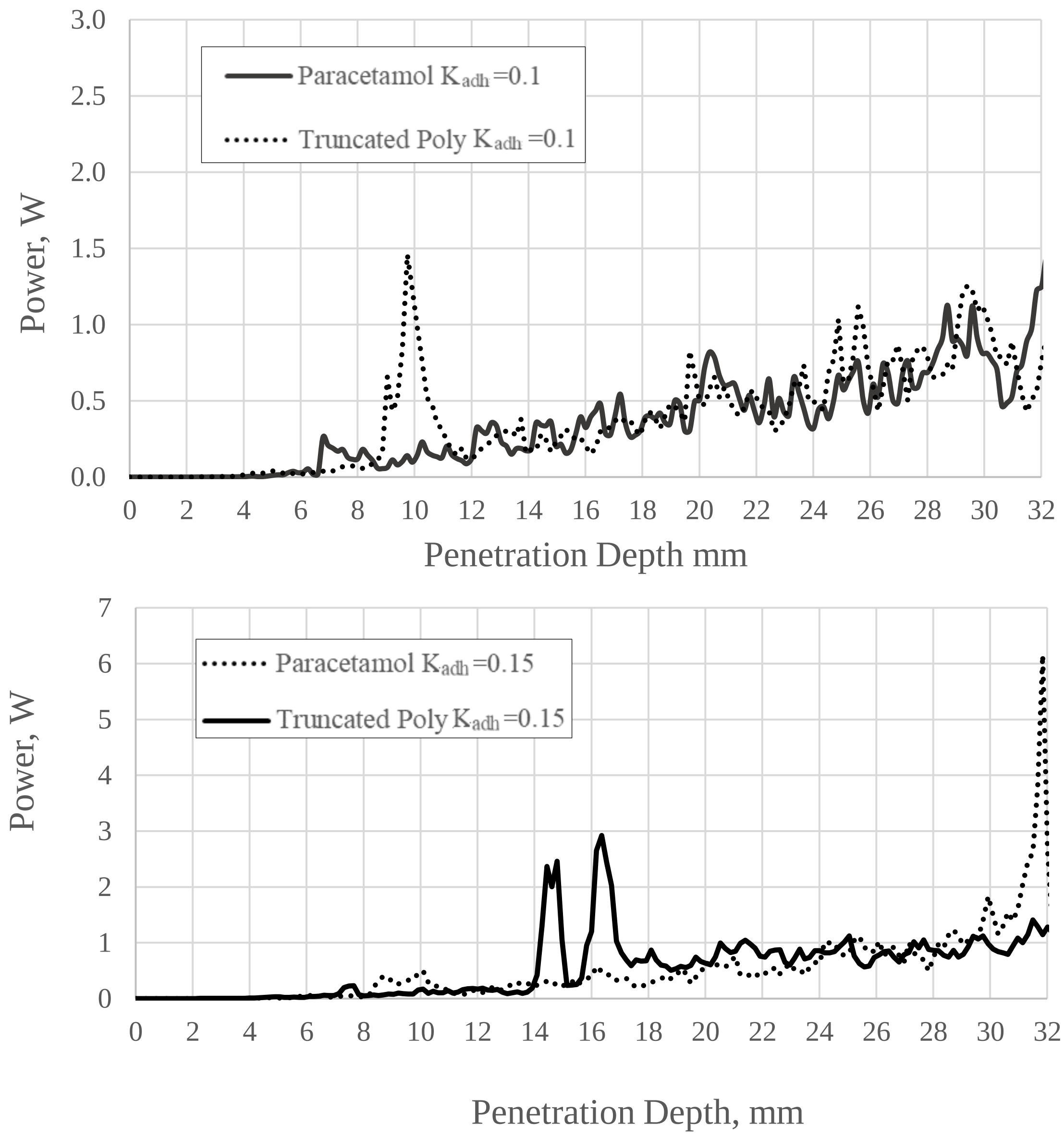

Figure 10: Comparison of power consumed by flow of truncated polyhedra and simulated paracetamol shapes at different levels of cohesion (25 mm vessel of the FT4 rheometer).

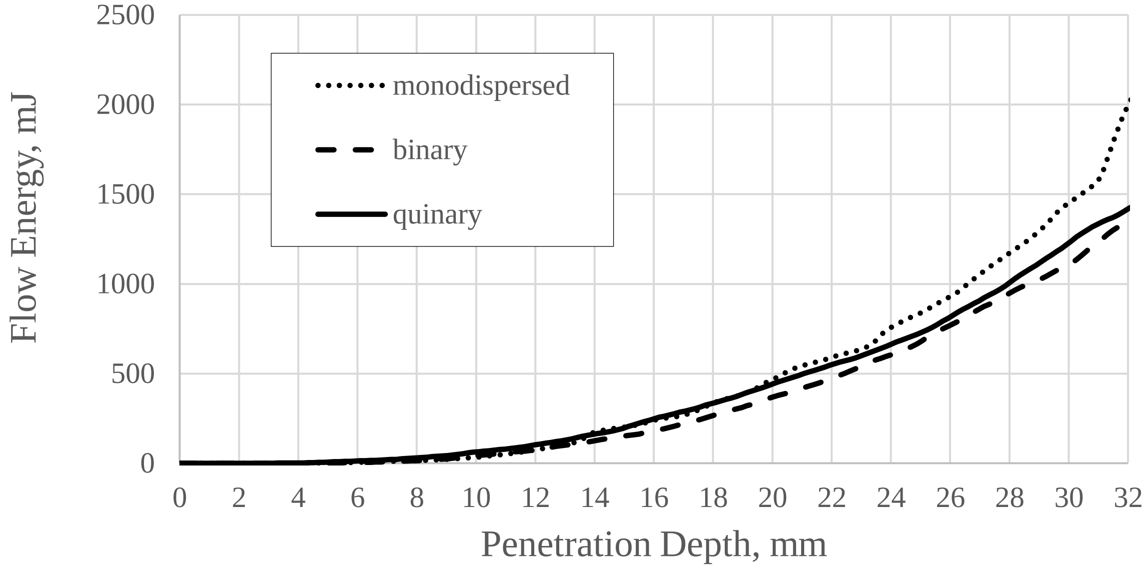

Figure 11: Comparison of flow energy of mixtures of truncated polyhedra with different surface energies. monodispersed: K_{adh}=0.1; binary: $K_{adh,1}$ =0.05, $K_{adh,2}$ =0.15; quinary= $K_{adh,1}$ =0.05, $K_{adh,2}$ =0.075, $K_{adh,3}$ =0.1, $K_{adh,4}$ =0.125, $K_{adh,5}$ =0.15 (25 mm vessel of the FT4 rheometer).

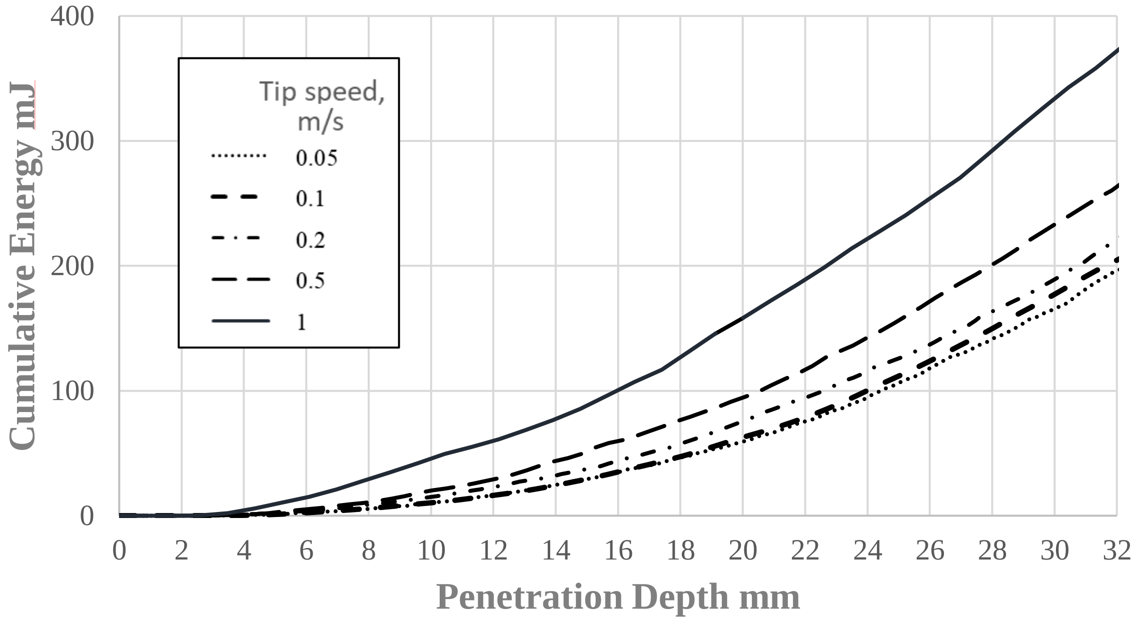

Figure 12: Effect of tip speed on the calculated flow energy for non-cohesive spheres (25mm vessel of the FT4 Rheometer).

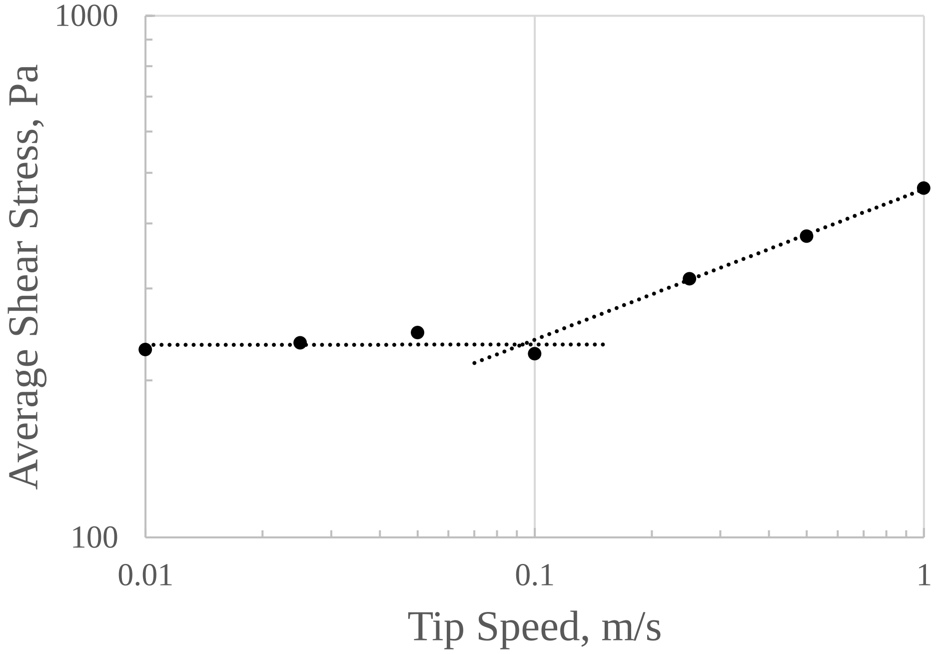

Figure 13: Variation of the average shear stress as a function of impeller tip speed for spheres.

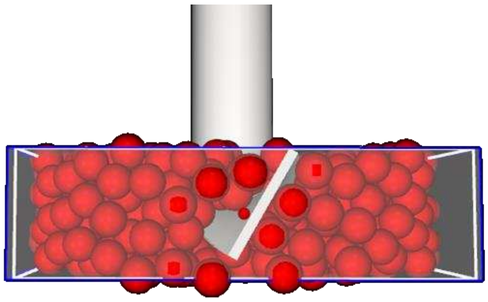

Figure 14: Averaging volume

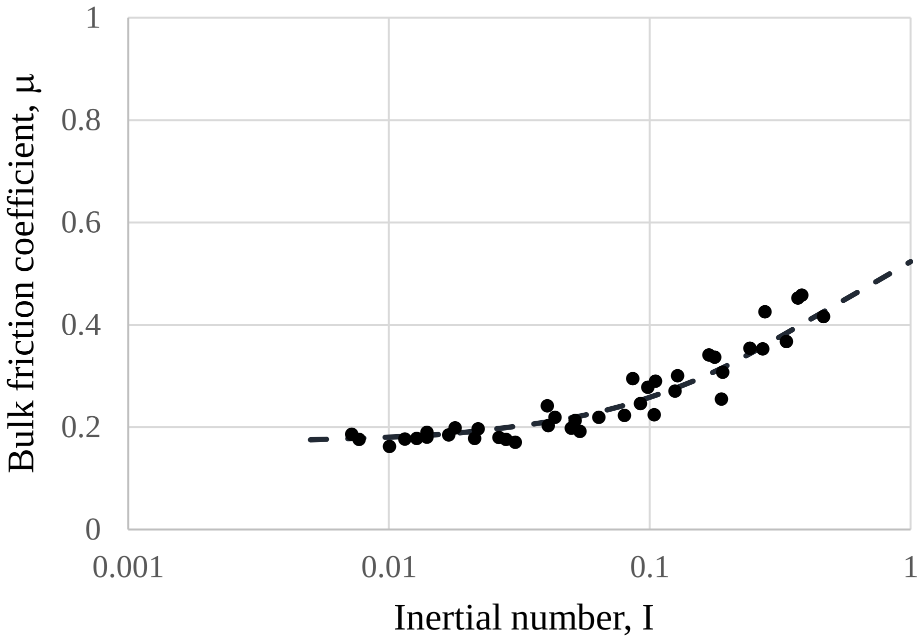

Figure 15: Bulk friction coefficient for non-cohesive spheres. Dotted line: Eq.(17) with μ_1=0.17, μ_2 = 0.7 and I_0=0.05.

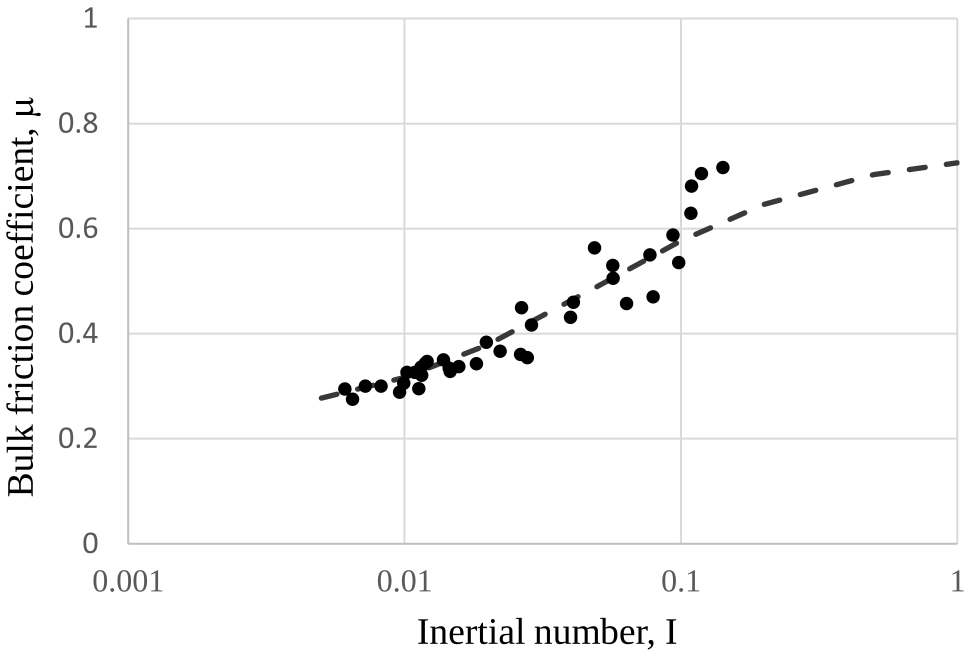

Figure 16: Bulk friction coefficient for non-cohesive deltahedra. Dotted line: Eq.(12) with μ_1=0.23, μ_2 = 0.75 and I_0=0.05.

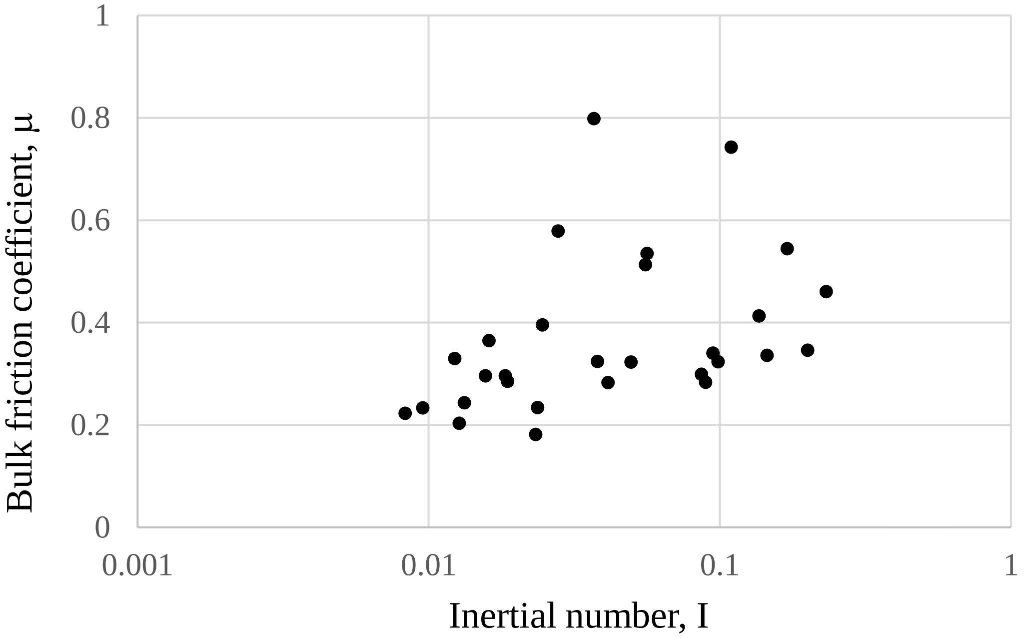

Figure 17: Bulk friction coefficient for cohesive spheres (K_{adh}=0.1).

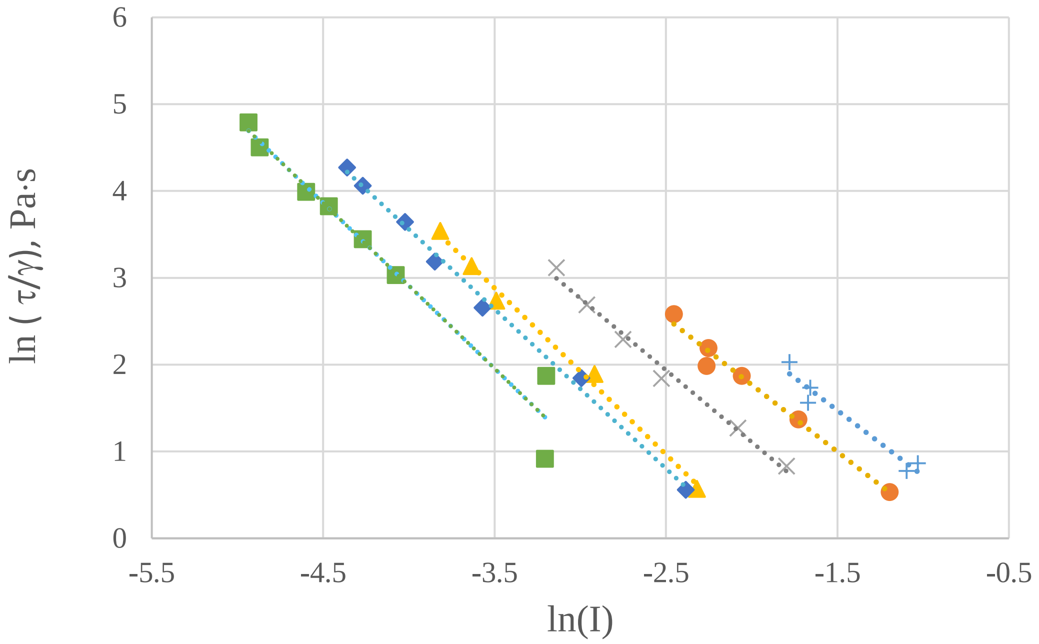

Figure 18: Apparent viscosity of non-cohesive spheres as a function of the inertial number for different tip speeds (25 mm vessel of the FT4 rheometer). Tip speed, m/s: + 1; ● 0.5; × 0.2; ▲ 0.1; ♦ 0.05; ■ 0.1.

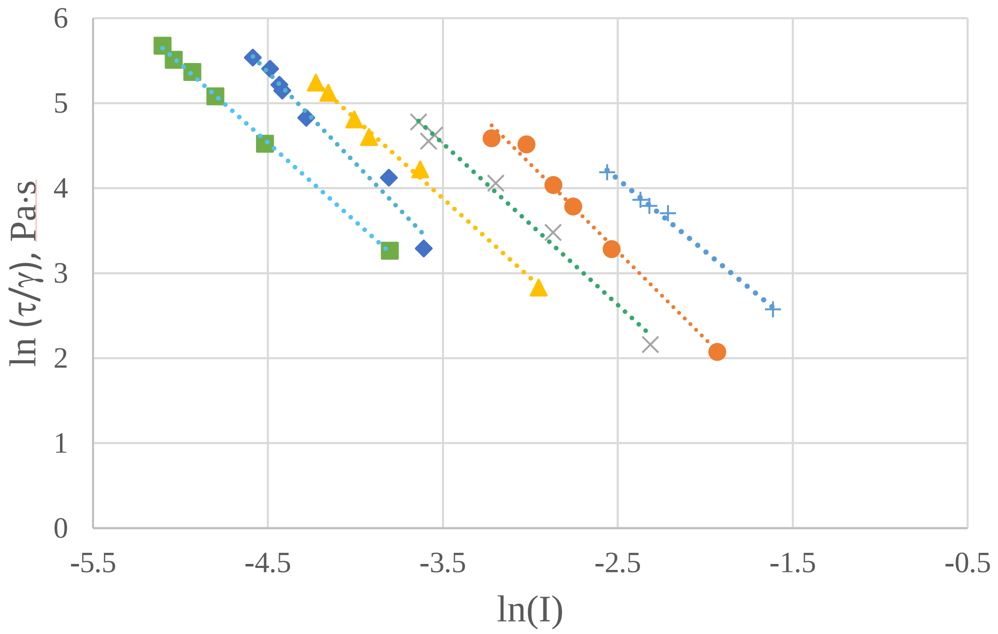

Figure 19: Apparent viscosity of non-cohesive deltahedra as a function of the inertial number for different tip speeds (25 mm vessel of the FT4 rheometer). Tip speed, m/s: + 1; ● 0.5; × 0.2; ▲ 0.1; ♦ 0.05; ■ 0.1.

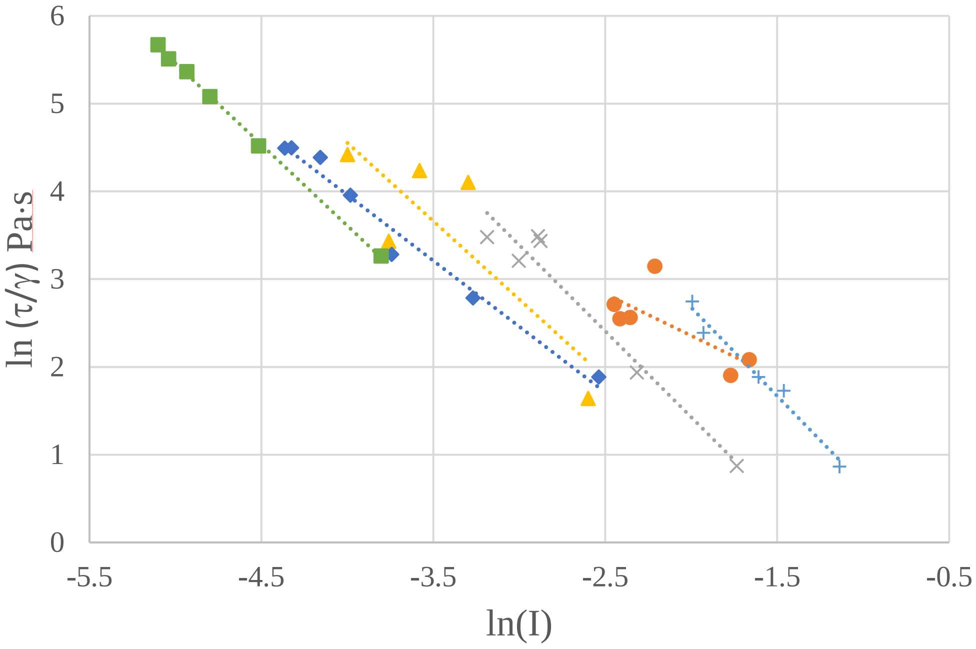

Figure 20: Apparent viscosity of cohesive spheres as a function of the inertial number at different values tip speeds (K_{adh}=0.1) (25 mm vessel of the FT4 rheometer). Tip speed, m/s: + 1; ● 0.5; × 0.2; ▲ 0.1; ♦ 0.05; ■ 0.1.

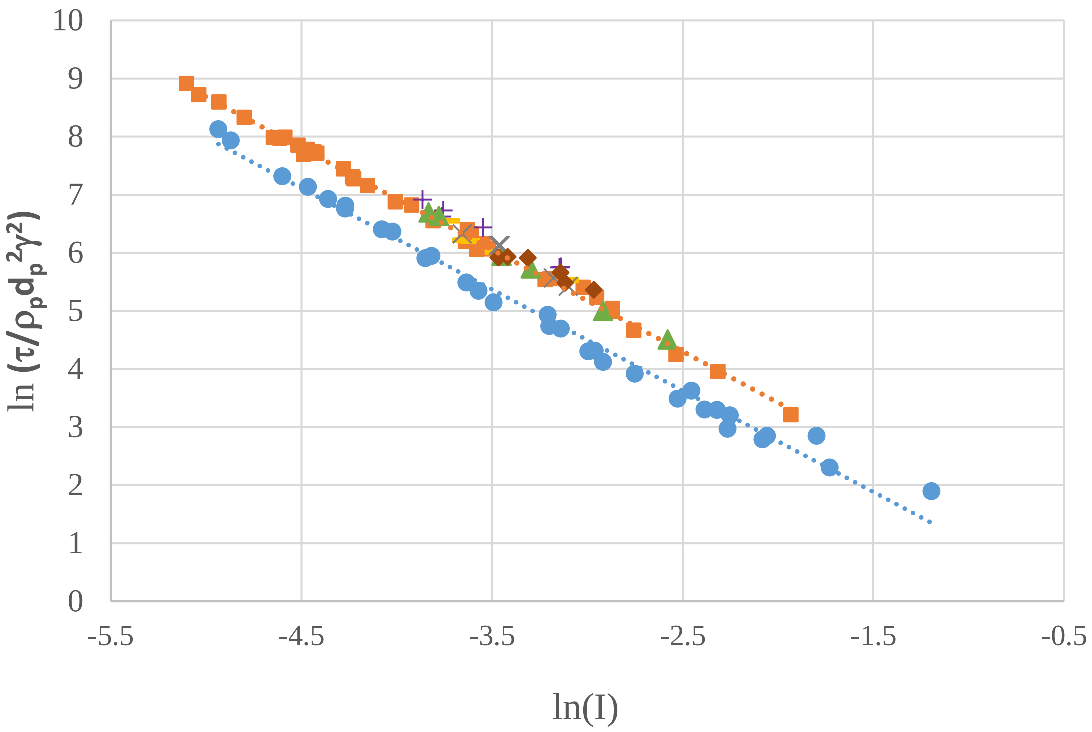

Figure 21: Dimensionless shear stress as a function of the inertial number for non-cohesive spheres and different types of faceted particles. Tip speed, m/s: • spheres; + faceted cylinder ; ■ deltahedra; ▲ paracetamol; × truncated polyhedra; – dodecahedra; ♦ truncated cube.

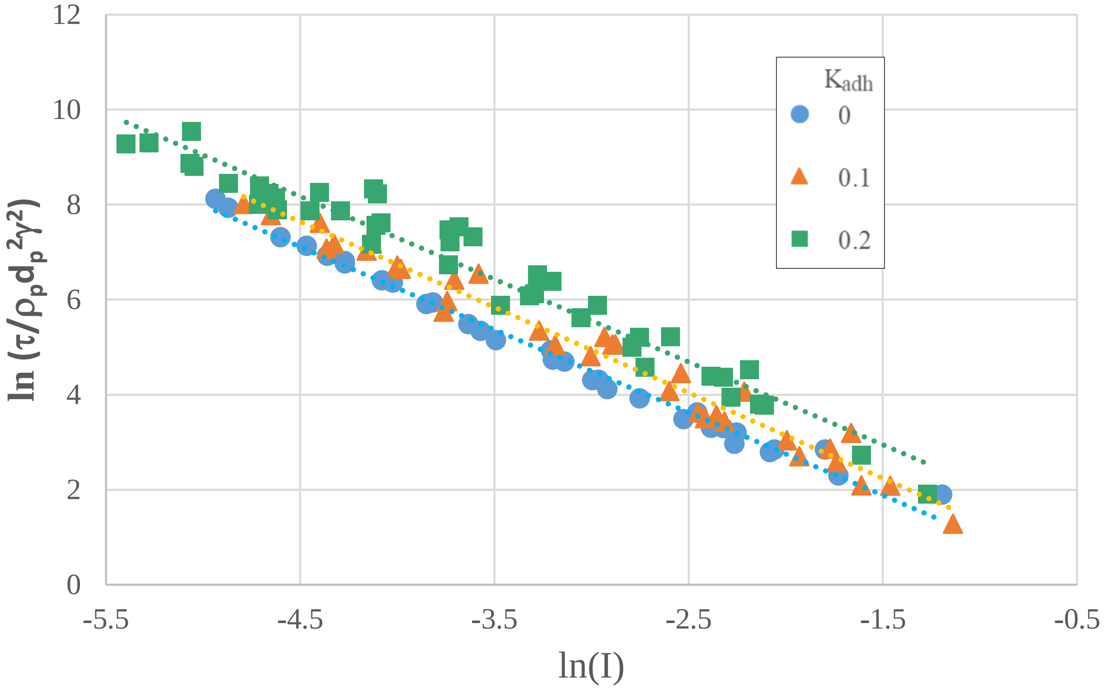

Figure 22: Dimensionless shear stress as a function of the inertial number for different adhesive stiffness values K_{adh}.